Evidence for prenucleated fibrilogenesis of acidmediated self-assembling oligopeptides via molecular simulation and fluorescence correlation spectroscopy

Lawrence R. Valverde, Bryce A. Thurston, Andrew L. Ferguson, and William L. Wilson

VALVERDE: ¹Department of Materials Science and Engineering, University of Illinois at Urbana-Champaign, 1304 West Green Street, Urbana, Illinois 61801, United States ²Frederick Seitz Materials Research Laboratory, University of Illinois at Urbana-Champaign, Urbana, Illinois 61801, United States

THURSTON: ¹Department of Materials Science and Engineering, University of Illinois at Urbana-Champaign, 1304 West Green Street, Urbana, Illinois 61801, United States

FERGUSON: ¹Department of Materials Science and Engineering, University of Illinois at Urbana-Champaign, 1304 West Green Street, Urbana, Illinois 61801, United States ²Department of Chemical and Biomolecular Engineering, University of Illinois at Urbana-Champaign, 600 South Mathews Avenue, Urbana, Illinois 61801, United States ³Department of Physics, University of Illinois at Urbana-Champaign, 1110 West Green Street, Urbana, Illinois 61801, United States ⁴Frederick Seitz Materials Research Laboratory, University of Illinois at Urbana-Champaign, Urbana, Illinois 61801, United States

WILSON: ¹Department of Materials Science and Engineering, University of Illinois at Urbana-Champaign, 1304 West Green Street, Urbana, Illinois 61801, United States ²Frederick Seitz Materials Research Laboratory, University of Illinois at Urbana-Champaign, Urbana, Illinois 61801, United States ³Center for Nanoscale Systems Faculty of Arts and Sciences Harvard University Cambridge, Massachusetts 02138, United States

Keywords: peptide aggregation; self-assembly; molecular dynamics; fluorescence correlation spectroscopy

ABSTRACT

An important step in controlling biomimetic amyloid systems is understanding the self-assembly reaction kinetics. We are interested in a family of such materials characterized by symmetric sequences of amino acids flanking a pi-conjugated functional core. Many of these materials rapidly self assemble into long fibers upon protonation in an acidic environment. Despite extensive investigation of these materials' properties, little is yet understood regarding their reaction kinetics. Based on previous studies we have chosen DFAG-4T-GAFD as a representative system and conducted molecular dynamics simulations to show that although large-scale assembly is induced by lowering pH, some degree of assembly is thermodynamically favorable in high-pH non-protonating environments. These results are consistent with findings for other systems such as DFAG-OPV-GAFD. The non-protonated aggregation also appears to be concentration dependent, occurring at concentrations of 100 nM and above. Single molecule measurements using fluorescence correlation spectroscopy provide experimental support for these computational predictions. We find evidence of spontaneous aggregation in aqueous solutions of peptides with concentrations as low as 100 nM; however, 10 nM solutions appear to be largely homogeneous solutions of unassembled monomer. These results indicate that the simplest explanations

for kinetics of acid-mediated assembly—protonation-induced nucleation by monomeric addition followed by subsequent stages of aggregation and elongation—are inappropriate in this system. In fact, the system only exists as pure monomer in very low concentrations, nucleation actually occurs in the absence of protonating elements at concentrations typically used for experiments, and pH triggered assembly proceeds from these preassembled aggregates. Accordingly, triggered assembly must be considered to operate outside the domain of nucleation-dependent models.

INTRODUCTION

Understanding the specific kinetics of assembly in amyloid-forming systems is a valuable step toward understanding how best to control such systems ¹. This is especially true in bio-inspired materials attempting to harness the potential of natural self-assembly to create functionalized devices with microscale or nanoscale order. Such biomimetic materials are researched for, and implemented in, a wide suite of applications ranging from cell growth and bioengineering 2 to photovoltaics 3. The synthetic oligopeptide system consisting of a pi-conjugated core flanked by symmetric sequences of amino acids has been explored in various permutations ^{2,4–7}, including recent work exploring the acid-mediated assembly of DFAG- π -GAFD, where π can be one of various pi-conjugated systems including quaterthiophene (4T), oligo(p-phenylene vinylene) (OPV3), and perylene-diimide (PDI). The piconjugated cores of these materials can be tuned for the specific applications desired, such as making ptype semiconductors with 4T and OPV3 cores and n-type with PDI. The pKa of the carboxyl terminus and C-terminal aspartic acid are 2.09 and 3.86, respectively⁸. Under the Henderson-Hasselbalch formalism, we can estimate that at pH 5 or higher the monomers are essentially completely deprotonated carrying a formal charge of (-4)e that precludes large-scale assembly by Coulombic repulsion. At pH 1 or lower they are essentially completely protonated and electrically neutral, eliminating the Coulombic repulsion and favoring assembly through van der Waals, hydrophobic, hydrogen bonding, and pi-pi stacking

interactions ⁹. Upon introduction to an acidic environment the titratable sites become fully protonated, and as a result peptide hydrophobicity, and peptide interaction via van der Waals forces, hydrogen bonding, hydrophobic interactions, and pi-pi stacking of the cores drive the peptides to assemble to form beta sheet-like aggregates ^{10,11}. Ideally these unassembled units would continue to stack in a ladder-like fashion with a helical twist (Figure 1A & 1B) ultimately forming long fibers. Although these fibers can be seen experimentally (Figure 1D), very little is understood about their assembly dynamics. Theoretical models suggest a variety of mechanisms by which these amyloid structures may form, with the classic example being an initial nucleation stage followed successive elongation stages. ^{12,13} However, reaction speed upon introduction of acid to this system has made characterization of the initial stages difficult.

In an effort to better understand the smaller-scale, early time assembly behaviors of DFAG, we have previously employed molecular dynamics simulations to probe the smaller-scale early time assembly behaviors of DFAG-OPV-GAFD peptides. Simulations have analyzed the impact of peptide symmetry, ¹⁰ concentration, ¹⁴ pH, and fluid flow ¹⁵ on assembly thermodynamics, kinetics, and morphology. We observed a strongly favorable free energy well at ~15 k_BT for the dimerization of DFAG-OPV3-GAFD peptide in a low pH environment. Addition of each subsequent monomer was found to yield a further decrease in free energy of ~25 k_BT , indicating that monomeric addition of peptides beyond dimerization is increasingly favorable. Our simulations suggest that aggregates at the free energy minima exist as well-aligned stacks with significant pi-stacking between cores. In addition, simulations probing the dynamics of assembly of protonated peptides beginning in the monomeric state indicated that peptides rapidly coalesce into spherical micelle-like structures, and then structurally ripen to form the well-ordered β -sheet stacks observed in free energy simulations on times scales larger than several tens of ns. The spontaneous formation of these self-assembled stacks in free energy simulations and the increasingly favorable changes in free energy upon further aggregation agree well with the suspected

amyloid-like nucleation and monomeric addition and elongation into larger 1-D fibers that have been observed experimentally. 4-6,9

Surprisingly, simulations of DFAG-OPV-GAFD under high-pH conditions also exhibited favorable dimerization with a change in free energy of ${}^{\sim}4k_BT$ due to hydrophobicity, pi-stacking, and dispersion interactions. Furthermore, the formation of higher order structures such as pentamers remain thermodynamically favorable with free energy change of ${}^{\sim}5k_BT$. These simulations suggest a paradigm in which early-stage assembly consists of light aggregates which rapidly assemble and subsequently reorganize into more thermodynamically stable beta-sheet-like structures, which in turn grow and elongate as further oligomeric units are added and structurally relaxed in a low-pH environment. The high-pH assembly predicted furthermore implies that when acid-mediated assembly is induced, the peptide precursor solution exists in a pre-nucleated state, significantly impacting how one should view the assembly kinetics in acid-mediated assembly experiments when analyzing through the lens of amyloid formation dynamics.

While most of the low-pH simulation observations support what has already been observed experimentally, ⁶ other work has provided support for the possibility of spontaneous assembly at high-pH ¹⁶. These recent microrheological observations demonstrate peptide assembly only down concentrations of 0.1 mM with no evidence of assembly below that concentration. This lack of experimental evidence is in large part due to the length scales and numbers of molecules under consideration. Microrheology relies on large, brightly fluorescing probes to correlate observed fluorescence with material properties. The microrheologically observed critical fiber formation concentration is likely due to limitations of the technique rather than actual physical phenomena. Thus, we have turned to fluorescence correlation spectroscopy (FCS), a single-molecule technique that allows us to directly detect peptide fluorescence to measure molecule size and to distinguish between low order aggregates of different sizes. Additionally, as our experiments utilized a close cousin of the

previously modeled peptides—DFAG flanking sequences with a quaterthiophene (4T) instead of oligo(p-phenylene vinylene)3 (OPV3)—we conducted additional simulations specific to the currently used peptide in order to verify consistency of the computationally observed phenomena.

EXPERIMENTAL METHODS

Fluorescence correlation spectroscopy allows single-molecule observation by confocally focusing a laser spot down to a femtoliter-scale volume (Figure 1C). As fluorescent molecules diffuse into and out of this volume, the fluctuations in fluorescence intensity observed can be time-correlated to gain information about the diffusion characteristics of the molecular species. Aggregates at different stages of self-assembly will of course have different sizes and mass, differences which are detected as they pass through the beam spot (Figure 1B and 1C), and can be extracted from the correlation data. The intensity fluctuations are related by means of a normalized autocorrelation function $G'(\tau)$:

$$G'(\tau) = 1 + \frac{\langle \delta F(0)\delta F(\tau)\rangle}{\langle F\rangle^2} \tag{1}$$

The autocovariance of F(t) is the autocorrelation function of the fluorescence fluctuations and is conventionally referred to as the "autocorrelation function," $G(\tau)$:

$$G(\tau) = \frac{\langle \delta F(0) \delta F(\tau) \rangle}{\langle F \rangle^2} \tag{2}$$

where F(t) is the fluorescence intensity at time t, and τ is the time between measured fluorescence events. The δ refers to the fluctuation in intensity relative to the average value. Further, the measured intensity can be written as a function of brightness, B; collection efficiency, CEF(r); excitation intensity, I(r); and the distribution of fluorophores, C(r,t):

$$F(t) = B \int CEF(r)I(r)C(r,t)dV$$
 (3)

For conventional one photon FCS, the confocal volume is isolated using an imaged pinhole. The experimental volume can be well approximated as a three-dimensional (3D) Gaussian ellipsoid with semi-minor axis—radius—r and semi-major axis—length—l. Assuming isotropic translational diffusion in such a volume for the distribution of fluorophores and plugging eq (3) into eq (2) yields an autocorrelation function:

$$G(\tau) = \frac{1}{N} \left(1 + \frac{\tau}{\tau_D} \right)^{-1} \left(1 + \left(\frac{r}{l} \right)^2 \frac{\tau}{\tau_D} \right)^{-1/2} \tag{4}$$

where N is the average number of particles in the observation volume, with 1/N being G(0), and τ_D is the diffusion time for the volume:

$$\tau_D = \frac{r^2}{4D} \tag{5}$$

The average fluorophore concentration can also be gleaned from N via the relation

$$\bar{C} = \frac{N}{V_{\text{eff}}} \tag{6}$$

where $V_{\rm eff}$ is the effective volume. This effective volume is different from the actual volume for an ellipsoid in that it represents the observation volume— $\pi^{3/2}r^2l$ for a 3D Gaussian—and it is critical to know this geometry to extract an accurate measure of the diffusion coefficient, D, from the diffusion time using eq (5). Thus, all FCS experiments are first calibrated by measuring the effective volume via a fluorophore with known diffusion coefficient. We used a ~1 nM aqueous solution of Rhodamine 110, with known $D \approx 340 \ \mu \text{m}^2 \text{s}^{-1}$ to calibrate the system each new day an experiment was run (see Supporting Information). 17,18 Other phenomena leading to signal depletion such as inter-system crossing to a triplet state, can be accounted for by incorporation into the correlation function. In general, these effects are

negligible to the phenomenon of interest and can be filtered out through time-bracketing of analyzed data. $^{19-21}$

Furthermore, as the effects of multiple species on the autocorrelation function is linear, multiple components can be accounted for by summing over all species such that

$$G(\tau) = \sum_{i=1}^{m} a_i \left(1 + \frac{\tau}{\tau_{Di}} \right)^{-1} \left(1 + \left(\frac{r}{l} \right)^2 \frac{\tau}{\tau_{Di}} \right)^{-\frac{1}{2}}$$
 (7)

and a_i represents the relative amplitude of each species.

Finally, while control of the confocal volume can be achieved using pinhole optics, two-photon illumination is often a better alternative when available. (Here the system is naturally confocal with volume defined by the nonlinear excitation dependence. Only molecules near the optical excitation focus contribute to the detected signal and no pinhole is needed.) Operating at such low concentrations increases the importance of each fluorescence photon and inclines the experimenter to use a larger pinhole aperture to reject fewer photons; however, as aperture increases so does the danger of optical artefacts skewing observations in ways that are mitigated by two-photon illumination, such as the false appearance of multiple species. ²² The illumination volume of a two-photon system is also advantageously smaller than the one photon case and is more accurately modeled by a 2D Gaussian in the plane of observation but a Lorentzian in the axial direction. It should be noted, though, that the Gaussian-Lorentzian model is a complicated solution without a closed form equation and can usually be approximated well enough by a 3D Gaussian for the sake of data analysis. ²³

All FCS experiments were performed on a Nikon Eclipse Ti inverted microscope equipped with an ISS

Alba FCS scanning mirror module, using a 60x (1.2 NA) water immersion lens. Pinhole confocal

experiments utilized a 470 nm diode laser with 3 mW power at the objective and two-photon excitation

was accomplished using a mode-locked Ti:Sapphire laser system (Tsunami and Millennia, Spectral

Physics) with 80 MHz pulse repetition rate and ~100 fs pulse width. The system has both a TCSPC board

and ISS FastFLIM card for time-tagged-time-resolved data acquisition. Autocorrelation functions were analyzed using the ISS Vista software. Samples were contained in μ -Slide 8-well glass slides (Ibidi). Wells coated with bovine serum albumin (BSA) or with aminosilane were compared to uncoated slides with no significant difference found. Thus, uncoated well slides were used for all experiments. Due to limitations of detectable fluorescence intensity, peptide concentrations below 10 nM were not investigated.

COMPUTATIONAL METHODS

For the generic aggregation process in which molecular species A and B form a complex AB

$$A + B \leftrightarrow AB$$

the thermodynamic equilibrium constant can be estimated from molecular simulation as ^{24,25}

$$K^{\Theta} = Kc^{\Theta} = \frac{1}{v^{\Theta}\sigma_{AB}} \int_{0}^{r_{b}} dr \, 4\pi r^{2} e^{-\beta F(r)} \tag{8}$$

where σ_{AB} is the symmetry number (2 for A=B, 1 otherwise), r_b is the center of mass cutoff distance below which an aggregate is considered to have formed, $\beta=(k_BT)^{-1}$, F(r) is the calculated potential of mean force at a center of mass separation value of r, and $c^{\Theta}=1/v^{\Theta}$ is the standard number concentration. The thermodynamic equilibrium constant may be related to the concentrations of the reactants and product as

$$K^{\Theta} = \frac{c^{\Theta}[AB]}{[A][B]} \tag{9}$$

where [X] is the number concentration of species X, $c^{\ominus}=1/v^{\ominus}$ is the standard concentration, and it is assumed that the system is sufficiently dilute that concentrations may be used instead of activities. So, by combining (8) and (9) and given the potential of mean force (PMF) for the aggregation of A and B to form complex AB, we can predict concentration equilibrium constants,

$$K = K^{\Theta} v^{\Theta} = \frac{[AB]}{[A][B]} = \frac{1}{\sigma_{AB}} \int_{0}^{r_{b}} dr \, 4\pi r^{2} e^{-\beta F(r)}$$
 (10)

For a system of monomeric self-assembly, by conservation of mass we have that the concentration of peptide in the system can be expressed as

$$[P] = [M] + 2[D] + 3[T] + \cdots$$
 (11)

where [P] is the total peptide concentration, [M] is the concentration of peptides that exist as monomers, [D] is the concentration of peptides that exist as dimers, [T] is the concentration of peptides that exist as trimers etc. From (10) and (11) we then have

$$[P] = [M] + 2K_2[M]^2 + 3K_2K_3[M]^3 + \cdots$$
 (12)

where K_2 is the equilibrium constant for the formation of dimers by $M+M\leftrightarrow D$, K_3 is the equilibrium constant for the formation of trimers by $D+M\leftrightarrow T$, etc. Eq (12) defines a polynomial in the peptide monomer concentration that can be solved for [M] and from which all higher aggregate concentrations can be computed using the calculated values of K_2 , K_3 , etc. ²⁶ For the peptides and concentrations investigated in this work, the equilibrium concentrations of aggregates heavier than six peptides are sufficiently low that the root of the polynomial is insensitive to truncation beyond the 6^{th} term, so it is only necessary to compute equilibrium constants for the hexamers and lighter aggregates. We have verified the insensitivity of the polynomial solution by incorporating terms up to 200 employing extrapolated equilibrium constants, and find that the computed value of [M] changes by less than 0.01%.

We use GROMACS 4.6.7 ^{27,28} to conduct all molecular dynamics simulations, with the AMBER99SB force field ^{29,30} and used the GlycoBioChem PRODRG2 Server ³¹ to obtain initial peptide geometries. The

terminal Asp residues and carboxyl termini were fully deprotonated to simulate a high pH (pH ≥ 5) environment in which each peptide carries a formal (-2)e charge at each terminus ^{8,9}. We conducted explicit solvent simulations in TIP3P water ³² with initial velocities generated from a Maxwell-Boltzmann distribution. Electrostatics were treated using the Particle Mesh Ewald scheme ³³ with a cutoff of 1.0 nm and a 0.12 nm Fourier grid spacing. Lennard-Jones interactions were smoothly shifted to zero at a cutoff of 1.0 nm. Bond lengths were fixed using the LINCS algorithm ³⁴, and Lorentz-Berthelot combining rules were used to determine interaction parameters between unlike atoms ³⁵. The system was integrated using the leap-frog algorithm with a 2 fs time step ³⁶.

Energy minimization was conducted using the method of steepest descents until the maximum force on any atom was less than 1000 kJ mol⁻¹ nm⁻¹. The system was then equilibrated in an NVT ensemble using a stochastic velocity rescaling thermostat ³⁷ to a constant temperature of 298 K. Further simulations were conducted in an NVT ensemble using a Nosé-Hoover thermostat ^{38,39} with a time constant of 0.5 ps.

Following our previous approach 9 we also conduct molecular dynamics simulations in implicit solvent with a modified model that rescales interactions to more accurately match explicit solvent. Polar interactions between solute and solvent are treated with the Generalized Born model while nonpolar interactions are implemented with a solvent accessible surface area approximation 40 . An analytical continuum electrostatic (ACE) type approximation 41 with a value of 2.259 kJ/mol.nm 2 for the surface tension 42 is made in treating nonpolar interactions. We calculated Born radii using the method of Onufriev, Bashford, and Case with a relative dielectric constant of 78.3 and with the standard parameter set of $\alpha = 1$, $\beta = 0.8$, and $\gamma = 4.85$ Since the peptides are not neutrally charged, implicit solvent simulations are conducted without the use of periodic boundary conditions. Coulombic and Lennard-Jones interactions are smoothly shifted to zero at the large cutoff value of 3.4 nm for the sake of stability.

We employed umbrella sampling 44 to compute the PMF as a function of center of mass separation between peptide aggregates. To compute the PMF for the formation of an n-mer from an (n-1)-mer and a monomer, the initial geometry of an n-mer aggregate is obtained by stacking n peptides at a core-core separation of 0.45 nm. The system was first equilibrated using the method of steepest descents until the maximum force on any given atom was less than 1000 kJ/mol.nm. Initial velocities of atoms were then drawn from a Maxwell-Boltzmann distribution and the system was equilibrated for 20 ps with the positions of the cores restrained in an NVT ensemble at a temperature of 298 K using a Langevin integrator as a thermostat with a friction constant of 0.5 ps^{-1 42}, and for another 20 ps with unrestrained cores under the same conditions. The system was then simulated for 1.5 ns and the configuration at the end of each 0.5 ns served as the initial configuration for a series of three independent simulations. Each initial configuration was then pulled both closer together and farther apart at a rate of 0.04 nm/ps using a harmonic biasing potential with a spring constant of 1000 kJ/mol.nm² between the center of mass of (n-1) peptides and the center of mass of the remaining monomer. These simulations were run for a sufficiently long time to allow the monomer to reach a distance from the (n-1)-mer at which the two were no longer able to interact. From these three separate pulling simulations, we then conducted three different umbrella sampling simulations by utilizing configurations over the course of each pulling simulation as the initial geometries for the restrained umbrella sampling. Windows were selected at evenly spaced intervals of 0.1 nm, were restrained using the same harmonic potential as the pulling simulation, and were run for 20 ns each. The first nanosecond of each simulation at each window was discarded to allow the system to equilibrate. We then used the weighted histogram analysis method (WHAM) 45,46 to reconstruct the unbiased PMF. Statistical errors in each PMF were computed using 100 bootstrap resamples of the data, and sampling errors were computed as the standard of deviation between each of the three umbrella runs. In each case, the $-2kT \log r$ non-interacting entropic contribution to the PMF was removed in order to give the PMFs a well-defined plateau and in order to

avoid double counting this entropic contribution which is already contained in the $4\pi r^2$ Jacobian of eq (10) 42,47 .

RESULTS AND DISCUSSION

Computing the PMF for the formation of aggregates of sizes 2-6 by means of monomeric addition at neutral pH (Figure 2), we observe free energy changes favoring aggregation on the order of $10 \, k_B T$ in each case. The dimerization of two peptides exhibits the largest free energy change at $\Delta F = (-15.2 \pm 1.1) \, k_B T$, while larger aggregates exhibit smaller free energy changes, although the formation of larger aggregates remains thermodynamically favorable. Despite repulsion between negatively charged termini, the minimum free energy configurations for each aggregate size exhibit a high degree of corecore stacking. Aggregates of 4 or fewer peptides also display a high degree of alignment in this stacking and frequently adopt linear stacks of parallel peptides. Aggregates of 5-6 peptides often favor configurations of 2-4 peptides existing in the same well aligned linear stacks with the remaining peptides stacking with one another. These results indicate that hydrophobic and pi-pi stacking interactions between the conjugated cores mean that it is favorable for peptides to form oligomeric aggregates even at neutral pH where the deprotonated Asp termini mediate substantial electrostatic repulsion.

The thermodynamics of self-assembling systems involve a nontrivial interaction between competing interactions ^{1,48}. Different interactions including hydrogen-bonding, pi-pi interactions, hydrophobic interactions, and entropy all contribute to the thermodynamics governing peptide assembly. In order to more fully understand some of these contributions to the aggregation of our system, we follow a similar approach to Ref. [⁹] and break the free energy of aggregation down into constituent components. In the implicit solvent systems studied, the change in free energy for the formation of an aggregate of size *n* may be written as:

$$\Delta F_n = \Delta U_n^{\rm intrapeptide} + \Delta U_n^{\rm peptide-peptide} + \Delta U_n^{\rm peptide-water} + \Delta U_n^{\rm water-water} - T \Delta S_n \tag{13}$$

where $\Delta U_n^{\rm intrapeptide}$ is the change in intramolecular peptide energy upon aggregation (including changes in intramolecular Lennard-Jones and Coulombic interactions, as well as angular stretching and dihedral torsions), $\Delta U_n^{\rm peptide-peptide}$ is the change in intermolecular interactions between peptides upon peptide association, $\Delta U_n^{\rm peptide-water}$ accounts for the change in dispersion and electrostatic interactions between peptide and solvent, $\Delta U_n^{\rm water-water}$ is the change in energy due to solvent-solvent interactions, T is the temperature, and ΔS_n accounts for the change in entropy of the system on aggregation. To elucidate different contributing factors, we divide peptide-peptide interactions into their Lennard-Jones and Coulombic components. The entropic contribution may be divided into changes in solvent entropy and changes in peptide entropy. Grouping all solvent related terms together, we define,

$$\Delta F_n^{\text{solvent}} \equiv \Delta U_n^{\text{peptide-water}} + \Delta U_n^{\text{water-water}} - T \Delta S_n^{\text{water}}. \tag{14}$$

Assuming that the peptide configurational entropy does not change substantially upon aggregation allowing us to neglect the entropy change of the peptides ⁹, we then have

$$\Delta F_n \approx \Delta U_n^{\rm intrapeptide} + \Delta U_n^{\rm peptide-peptide\,LJ} + \Delta U_n^{\rm peptide-peptide\,Coulomb} + \Delta F_n^{\rm solvent}. \tag{15}$$

The change in free energy ΔF_n on the left-hand side is precisely the well depth of the PMF computed by umbrella sampling. The three energetic terms on the right-hand side $\Delta U_n^{\rm intrapeptide}$, $\Delta U_n^{\rm peptide-peptide\ LJ}, \text{ and } \Delta U_n^{\rm peptide-peptide\ Coulomb} \text{ can be computed directly from our simulations from}$

the energies of the various aggregate sizes averaged over 20 ns unbiased MD simulations. The solvent contributions $\Delta F_n^{\rm solvent}$ follow from the residual on the right-hand side of eq 15.

We illustrate the results of this analysis for peptide aggregates ranging from two to six peptides in Figure 3. For each aggregate size we observe small favorable contributions in both intrapeptide interaction and \Box interaction between peptides. As anticipated, the most significant unfavorable contribution is due to Coulombic repulsion, but that this is balanced by a large favorable solvent contribution and smaller favorable dispersion and intrapeptide energetic contributions. We do observe that this decomposition was computed for an implicit solvent model, and that a more detailed analysis would employ a fully explicit solvent model with a polarizable force field.

From eq (10), the equilibrium constants for the formation of aggregates are computed from these PMFs along with 90% confidence intervals (Table 1). Confidence intervals are estimated by randomly generating 10⁶ PMFs by shifting each point on the PMF by the product of the bootstrap error at that point with a single number randomly generated from a Gaussian distribution with zero mean and unit standard deviation. Each PMF is then integrated over the binding region to obtain 10⁶ different values for each equilibrium constant, the middle 90% of which defines the confidence interval.

Despite the favorable PMFs, low overall peptide concentrations favor light aggregate distributions. From eqs (10) and (12), we calculate the predicted distribution of aggregate sizes in deprotonated peptides from the computed PMFs based on the overall peptide concentration (Figure 4). Error estimates are obtained by randomly sampling equilibrium constants within the 90% confidence intervals. We predict that at a concentration of 10 nM the vast majority (~96%) of the peptide tends to exist as isolated monomers. When the peptide concentration is increased to 100 nM we observe a significant shift in the distribution of peptide sizes that indicates an appreciable amount of aggregation

of peptide into larger aggregates, including dimers (22%) and trimers (2%). Such a transition is in qualitative agreement with what is observed experimentally.

Measurements of peptide in aqueous solution at 10 nM reveal diffusion coefficients on average (300 \pm 50) μ m²s⁻¹ (Figure 5C, Table 2). These are consistent with particles on the order of 1 nm assuming the Stokes-Einstein equation,

$$r_h = \frac{kT}{6\pi\eta D} \tag{13}$$

provides a reasonable underestimate of particle size, where r_h is the hydrodynamic radius, k_B is Boltzmann's constant, T is the temperature, η represents the fluid viscosity, and D is the diffusion constant. As an added check, we utilize explicit solvent molecular dynamics simulations to compute the diffusion constant of the peptide monomer by means of the Einstein diffusion equation

$$\frac{\partial \langle r^2(t) \rangle}{\partial t} = 2dD \tag{14}$$

where $\langle r^2(t) \rangle$ is the mean-squared-deviation (MSD) of the molecule as a function of lag time, and d is the dimensionality of the system. A 50 ns unbiased simulation is conducted, the first ns of which is ignored to allow the system to equilibrate, and the diffusion constant computed from the slope of the linear regime of the MSD. The diffusion constant for peptide monomers is computed to be (330 ± 10) μ m²/s⁴², in good agreement with experiment. Furthermore, the measured concentrations for these diffusion coefficients are ~1.78±0.36 nM, which correspond reasonably well with the intended concentrations when achieved by manually pipetted dilutions.

Interestingly, peptide solutions of concentrations ten times greater, at 100 nM, can often no longer be fit to a 1-species autocorrelation model. Furthermore, when fitting data to 2-species models we find average diffusion coefficients ranging from \sim 0.1 to \sim 5 to \sim 500 μ m²s⁻¹, often with the same species overlapping multiple datasets (Figure 5A & 5B). These correspond to particles ranging in size from

monomeric to 1000 times larger coexisting within the sample volume. Thus, we are able to experimentally support computational predictions that at concentrations as low as 100 nM the peptides spontaneously assemble small aggregates even in the absence of a protonating acid solution.

The discrepancy in aggregate sizes between simulation predictions and experimental measurements is understandable given that this computational approach does not account for all possible mechanisms of aggregate formation. The method utilized in computing equilibrium constants implicitly assumes that *n*-mers are formed only by the addition of a monomer to a pre-existing, tightly bound (*n*-1)-mer; it does not allow for the possibility of a chain of weakly interacting, smaller aggregates despite the previously established importance of these alternate assembly pathways ^{12,13,49}. These predictions of aggregate sizes then only include tightly stacked aggregates, and thus we expect this treatment to be useful in quantifying well-aligned aggregates, but to underestimate aggregate sizes by ignoring the existence of large, weakly interacting networks of peptide oligomers.

Finally, when acid is directly added to any of the aforementioned solutions the result is a rapid and dramatic fluorescence quenching and decrease in the *G*(0) intercept of the autocorrelation curves, indicating a rise in measured concentration. While these effects are apparently contradictory—with quenching associated with assembly but assembly associated with decreased concentration—we are inclined to conclude that assembly occurs, given the known phenomenon of quenching as a result of assembly and assembly being triggered or significantly catalyzed by the addition of acid. Meanwhile, an alternative explanation for the increased concentration is readily available in consideration of the decreased fluorescence signal. The decreased fluorescence intensity also dramatically lowers the signal to noise ratio, making it likely that the correlations observed are artefacts of the system rather than true events. For this reason, autocorrelation fitting and derived parameters are not provided for these curves. Thus, the FCS data for these ultra-low concentration solutions nicely overlap with computational predictions, indicating that the peptide exists in a monomeric state in non-protonating conditions at

concentrations of 10 nM and lower. While the rapidity of acid-triggered assembly has precluded the detection of any lag phase, computations in this work as well as prior coarse-grained simulation work corroborate the lack of a lag phase ¹⁴. The spatial and temporal multiscale nature of systems such as those discussed in this work often necessitate computational methods to characterize kinetics due to the intractability of experimental probing. Thus, it is particularly valuable when experimental measurements are available to bolster conclusions that are computationally derived from theoretical hypotheses ⁴⁸. In this instance, simulation indicates that nucleation-dependent models are unlikely to accurately reflect this system's kinetics. Finally, experimental results from FCS indicate, in agreement with simulation, that assembly is not truly acid-triggered, but rather acid-mediated, and the fibrils formed upon introduction of acid initiate from a pre-nucleated state.

Given the above observations, it is reasonable to generalize our findings to any acid-mediated system that also relies upon hydrophobic and/or pi-pi interactions for self-assembly. In any such case, the driving forces for assembly always exist and the true role of protonation is to further lower the energy barrier to these mechanisms by counteracting electrostatic counterforces to assembly. Thus, we expect any aid-triggered system with synergistic avenues for self-assembly such as hydrophobic, pi-pi, or other van der Waals interactions to be in actuality an acid-mediated system beginning in a pre-nucleated state.

Finally, it may be possible to further substantiate these conclusions through further experimental and data analysis techniques. Electrospray ionization mass spectrometry (ESI-MS) of the system could be employed for the system with concentrations varying between 10 nM and higher than 100 nM, and the specific role of hydrophobicity in the nucleation stage might be further investigated through the use of ionic liquids in lieu of deionized water ⁵⁰. It may also be possible to achieve greater detail regarding the diversity of oligomer sizes produced through spontaneous nucleation at various pH through the use of maximum entropy analysis of the FCS data ^{51–56}.

CONCLUSIONS

We have conducted molecular dynamics simulations to confirm the consistency of assembly behavior between previously computer DFAG-OPV3-GAFD peptides and their DFAG-4T-GAFD cousins. These simulations demonstrate that for both materials, not only is macroscopically observable assembly triggered by lowering a solution's pH, but also even in non-protonating environments some degree of aggregation is thermodynamically favorable. Single molecule measurements using fluorescence correlation spectroscopy provide experimental support for these computational predictions. We find that aqueous solutions of peptides in concentrations as low as 100 nM will spontaneously aggregate to form heterogeneous solutions with sizes ranging from monomeric to 1000 times larger. However, below 100 nM solutions appear to be homogeneous solutions of unassembled monomer. These results indicate that previously assumed paradigms of acid-mediated assembly in this system whereby monomer aggregates upon protonation were incomplete. In fact, the system only exists as pure monomer in very low concentrations, and under experimental conditions the high-pH untriggered solution already exists in a pre-nucleated state.

Table 1. Equilibrium constants for the formation of an aggregate of size n from a tightly-bound (n-1)-mer and a monomer.

Aggregate size	Equilibrium constant, K (M ⁻¹)	90% confidence Interval, (M ⁻¹)
2	1.8×10 ⁶	(5.1×10 ⁵ , 6.4×10 ⁶)
3	6.6×10 ⁵	(1.2×10 ⁵ , 3.9×10 ⁶)
4	4.7×10 ⁴	(4.9×10 ³ , 4.7×10 ⁵)
5	2.8×10 ⁴	(3.9×10 ³ , 2.1×10 ⁵)
6	1.0×10 ⁵	(9.7×10 ³ , 1.1×10 ⁶)

Table 2. Comparing values for 10 nM vs 100 nM.^a

Sample		D (um2/s)	C (nM)	Percent of Solution
10 nM Solution		191	2.29	
		320	1.42	
		317	1.59	
		288	2.14	
		338	1.48	
		325	1.75	
100 nM Solution	Species 1	3.78	0.0229	
		4.31	0.0563	
		4.05	0.0597	
		4.94	3.12	
		6.33	3.09	
		5.01	3.07	
	Species 2	0.125		85.7 %
		0.0193		77.0 %
		0.162		81.1 %
		651		49.1 %
		337		41.8 %
		446		40.8 %

a Data from six FCS curves each are shown for 10 nM and 100 nM samples. The 10 nM data are fit with one species for each curve and thus show one value for each of the six curves under the diffusion coefficient (D) and concentration (C) columns. The 100 nM solutions are fit using two species, with one diffusion coefficient tabulated in each of the "Species 1" rows and the other in each of the "Species 2" rows. Meanwhile concentrations for the 100 nM data are tabulated for each dataset's species 1. And for each species 2, its percentage of the total solution is tabulated in the last column.

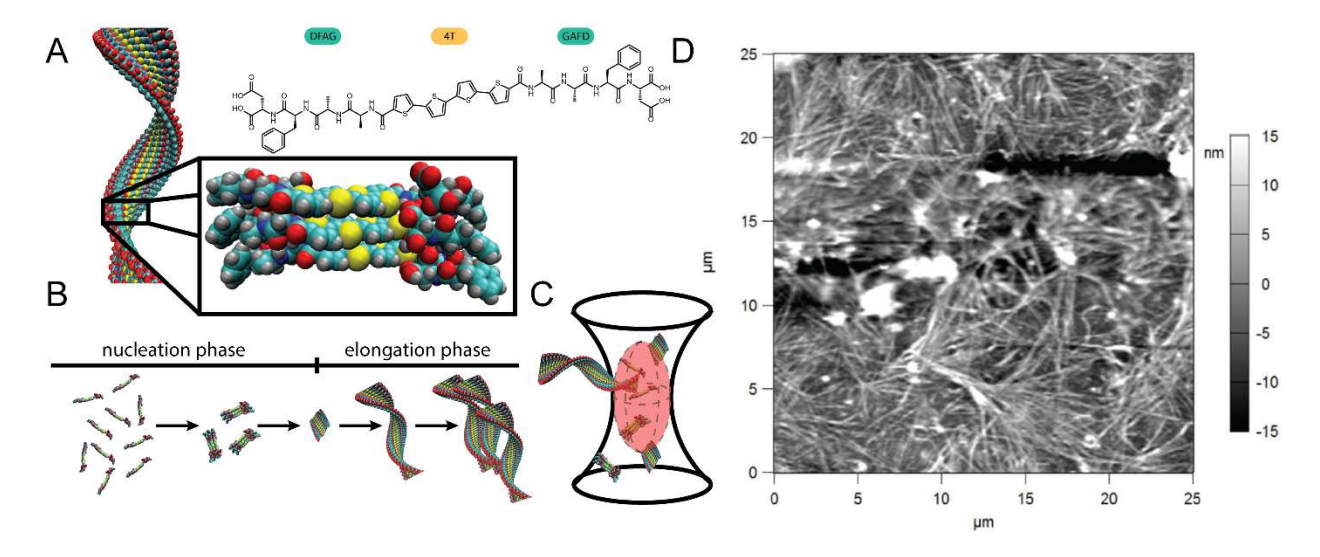


Figure 1. Illustration of DFAG-4T structure, aggregation, and FCS detection. A) Chemical structure and idealized stacking behavior of DFAG-4T. B) Standard model for amyloid formation via nucleation-dependent aggregation. C) Confocal spot and observation volume (ellipsoid) used for FCS. As aggregates of various sizes pass into and out of the observation volume fluctuations in fluorescence intensity are detected. D) Atomic Force Microscope (AFM) image of DFAG-4T fibers deposited on Si.

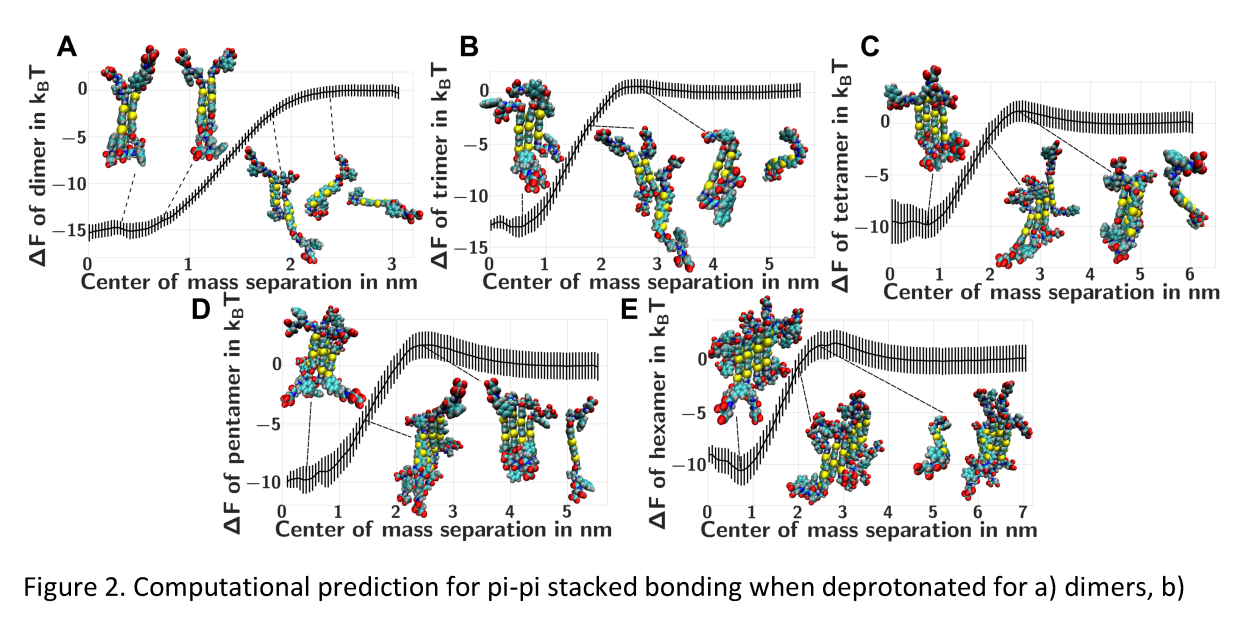


Figure 2. Computational prediction for pi-pi stacked bonding when deprotonated for a) dimers, b) trimers, c) tetramers, d) pentamers, and e) hexamers with representative configurations of aggregates at various points along the reaction coordinate.

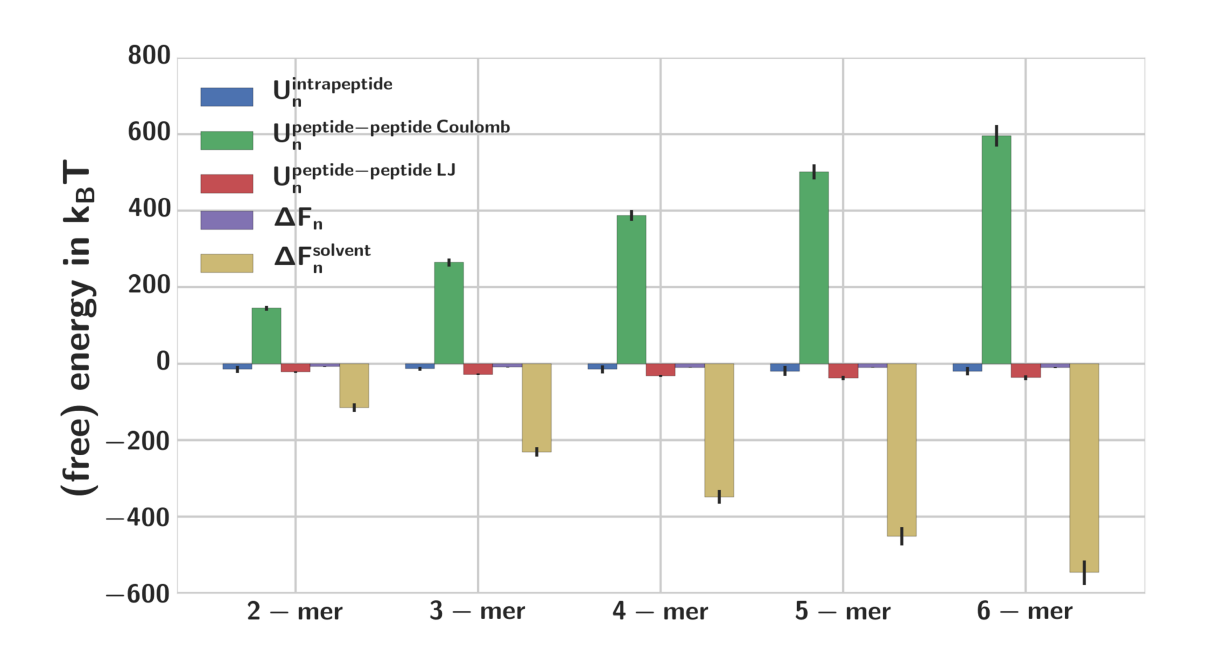


Figure 3. Decomposition of the free energy of association ΔF_n into energetic and solvent-mediated contributions for n=(1-6)-mers (eqs. 13-15). The strongly unfavorable Coulombic repulsion $\Delta U_n^{\mathrm{peptide-peptide Coulomb}}$ is balanced by a favorable solvent-mediated term $\Delta F_n^{\mathrm{solvent}}$.

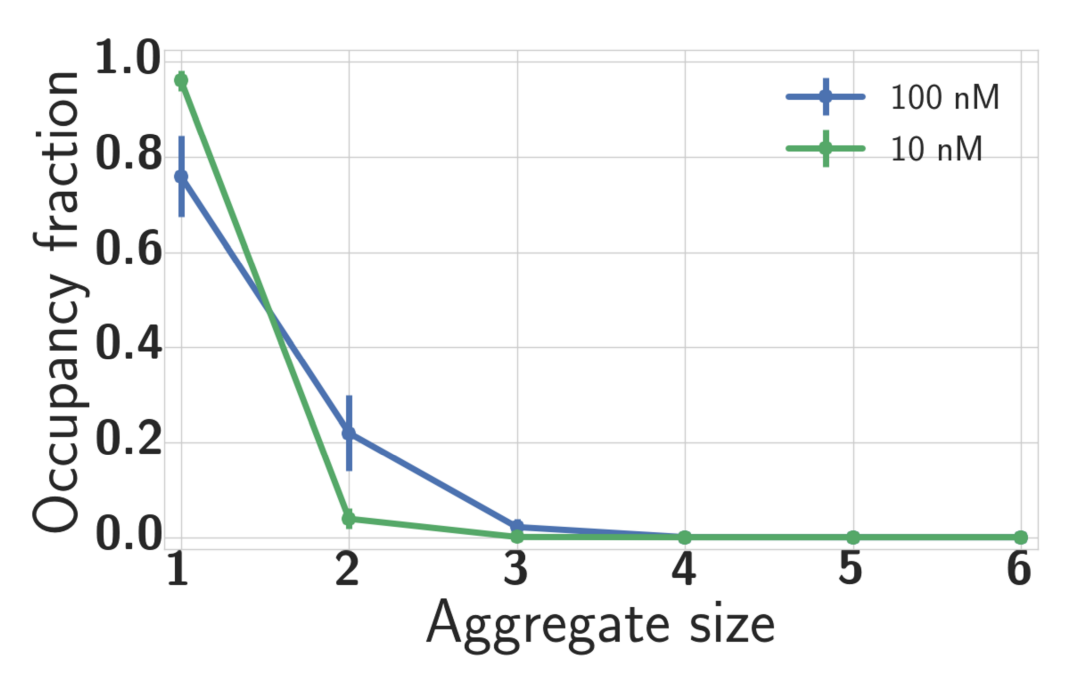


Figure 4. Predicted fraction of peptide existing in various aggregate sizes at peptide concentrations of 10 nM (green) and 100 nM (blue). Lines are drawn to guide the eyes. Error bars are estimated by random sampling of K values within the 90% confidence interval.

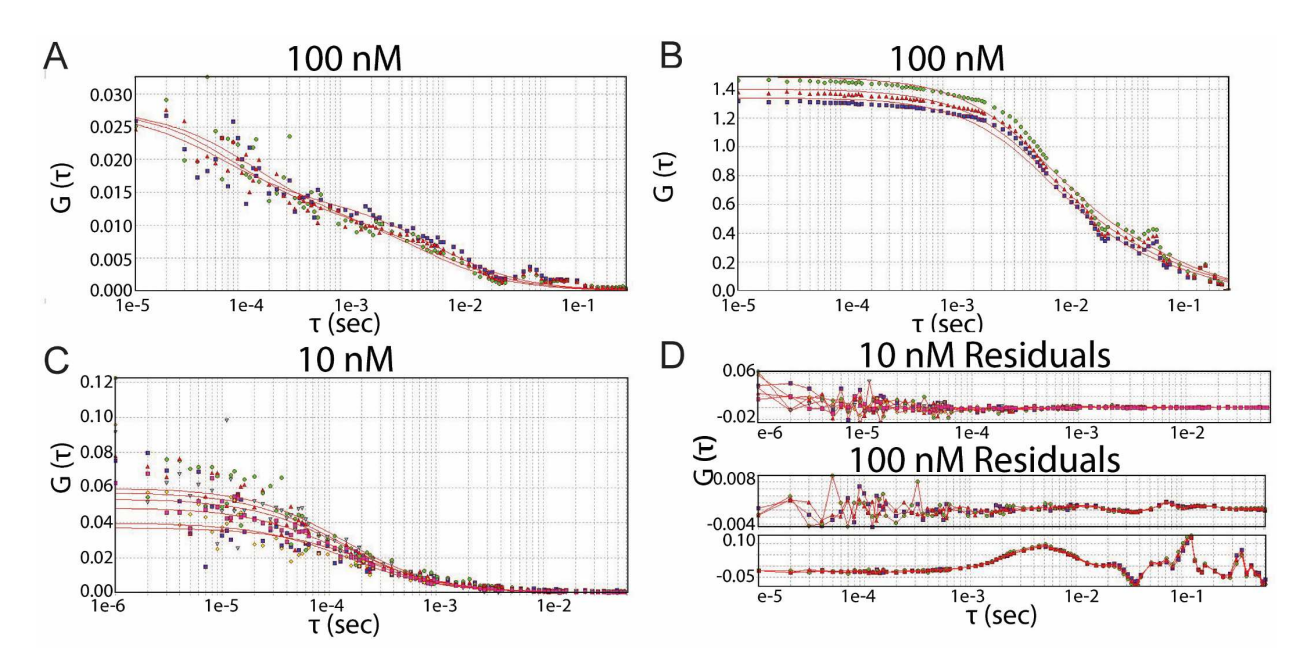


Figure 5. FCS data for comparison of 10 nM vs 100 nM samples. A) Three experiments at 100 nM B)

Three other experiments also at 100 nM illustrate how data from the same sample can look very different depending on the sizes of species passing through the confocal volume. C) Six experiments at 10 nM, demonstrating sample homogeneity. D) Residuals for the fitted curves in (A)-(C).

Corresponding Author

WILSON: Center for Nanoscale Systems Faculty of Arts and Sciences Harvard University 11 Oxford St., LISE 308 Cambridge, Massachusetts 02138, United States, wwilson@fas.harvard.edu

Author Contributions

The manuscript was written through contributions of all authors. All authors have given approval to the final version of the manuscript.

ACKNOWLEDGEMENTS

Research supported by the U.S. Department of Energy (DOE), Office of Science, Basic Energy Sciences (BES), under Award # SC-0011847 (experimental studies) and by the National Science Foundation (NSF) under Grant No. DMR-1729011 (computational studies). We thank Dr. J. D. Tovar and Tejaswini Kale for providing the peptide material for this study and Gianni Pezzarossi for use of computational resources. We also thank the Frederick Seitz Materials Research Laboratory, the Beckman Institute for Advanced Science and Technology, and the Carl R. Woese Institute for Genomic Biology for facilities and instrumentation.

REFERENCES

- (1) Wang, J.; Liu, K.; Xing, R.; Yan, X. Peptide Self-Assembly: Thermodynamics and Kinetics. *Chemical Society Reviews* **2016**, *45*, 5589–5604.
- (2) Diegelmann, S.; Gorham, J.; Tovar, J. One-Dimensional Optoelectronic Nanostructures Derived from the Aqueous Self-Assembly of Π-Conjugated Oligopeptides. *Journal of the American Chemical Society* **2008**, *130*, 13840–13841.
- (3) Wall, B.; Diegelmann, S.; Zhang, S.; Dawidczyk, T.; Wilson, W.; Katz, H.; Mao, H.; Tovar, J. Aligned Macroscopic Domains of Optoelectronic Nanostructures Prepared via Shear-Flow Assembly of Peptide Hydrogels. *Advanced Materials* **2011**, *23*, 5009–5014.
- (4) Tovar, J. Supramolecular Construction of Optoelectronic Biomaterials. *Accounts of chemical research* **2013**, *46*, 1527–1537.
- (5) Wall, B.; Tovar, J. Synthesis and Characterization of Π-Conjugated Peptide-Based Supramolecular Materials. *Pure and Applied Chemistry* **2012**, *84*, 1039–1045.
- (6) Marciel, A. B.; Tanyeri, M.; Wall, B. D.; Tovar, J. D.; Schroeder, C. M.; Wilson, W. L. Fluidic-Directed Assembly of Aligned Oligopeptides with π-Conjugated Cores. *Advanced Materials* **2013**, *25*, 6398–6404.
- (7) Ardoña, H.; Tovar Energy Transfer within Responsive Pi-Conjugated Coassembled Peptide-Based Nanostructures in Aqueous Environments. **2015**.
- (8) Campbell, M. K.; Farrell, S. O. *Biochemistry*; 8th ed.; Cengage Learning: Stamford, CT, 2014.
- (9) Thurston, B.; Tovar, J.; Ferguson, A. Thermodynamics, Morphology, and Kinetics of Early-Stage Self-Assembly of Π-Conjugated Oligopeptides. *Molecular Simulation* **2016**, *42*, 955–975

- (10) Wall, B.; Zhou, Y.; Mei, S.; Ardoña, H.; Ferguson, A.; Tovar, J. Variation of Formal Hydrogen-Bonding Networks within Electronically Delocalized Π-Conjugated Oligopeptide Nanostructures. *Langmuir* **2014**, *30*, 11375–11385.
- (11) Wall, B.; Zacca, A.; Sanders, A.; Wilson, W.; Ferguson, A.; Tovar, J. Supramolecular Polymorphism: Tunable Electronic Interactions within Π-Conjugated Peptide Nanostructures Dictated by Primary Amino Acid Sequence. *Langmuir* **2014**, *30*, 5946–5956.
- (12) Michaels, T.; Knowles, T. Mean-Field Master Equation Formalism for Biofilament Growth. *American Journal of Physics* **2014**, *82*, 476–483.
- (13) Cohen, S.; Vendruscolo, M; Dobson, CM The Kinetics and Mechanisms of Amyloid Formation. *Amyloid Fibrils and* ... **2013**.
- (14) Mansbach, R.; Ferguson, A. Coarse-Grained Molecular Simulation of the Hierarchical Self-Assembly of Π-Conjugated Optoelectronic Peptides. *The Journal of Physical Chemistry B* **2017**.
- (15) Mansbach, R.; Ferguson, A. Control of the Hierarchical Assembly of -Conjugated Optoelectronic Peptides by pH and Flow. *Organic & Biomolecular Chemistry* **2017**.
- (16) Zhou, Y.; Li, B.; Li, S.; Ardoña, H.; Wilson, W.; Tovar, J.; Schroeder, C. Concentration-Driven Assembly and Sol–Gel Transition of Π-Conjugated Oligopeptides. *ACS Central Science* **2017**.
- (17) Gendron; Avaltroni; Wilkinson Diffusion Coefficients of Several Rhodamine Derivatives as Determined by Pulsed Field Gradient–nuclear Magnetic Resonance and Fluorescence Correlation Spectroscopy. **2008**.
- (18) Kapusta, P. Absolute Diffusion Coefficients: Compliation of Reference Data for FCS Calibration.

- (19) Enderlein, J.; Gregor, I.; Patra, D.; Fitter, J. Art and Artefacts of Fluorescence Correlation Spectroscopy. *Current pharmaceutical biotechnology* **2004**, *5*, 155–161.
- (20) Enderlein, J.; Gregor, I.; Patra, D.; Fitter Art and Artefacts of Fluorescence Correlation Spectroscopy. *Current Pharmaceutical Biotechnology* **2004**, *5*, 155–161.
- (21) Grunwald; Cardoso; Leonhardt Diffusion and Binding Properties Investigated by Fluorescence Correlation Spectroscopy (FCS). **2005**.
- (22) Hess, S.; Webb, W. Focal Volume Optics and Experimental Artifacts in Confocal Fluorescence Correlation Spectroscopy. *Biophysical Journal* **2002**, *83*, 2300–2317.
- (23) Nagy, A.; Wu, J.; Berland, K. Observation Volumes and Γ-Factors in Two-Photon Fluorescence Fluctuation Spectroscopy. *Biophys J* **2005**, *89*, 2077–2090.
- (24) Jeon, J.; Shell, S. Charge Effects on the Fibril-Forming Peptide KTVIIE: A Two-Dimensional Replica Exchange Simulation Study. *Biophysical Journal* **2012**, *102*, 1952–1960.
- (25) Gilson, M. K.; Given, J. A.; Bush, B. L.; McCammon, J. A. The Statistical-Thermodynamic Basis for Computation of Binding Affinities: A Critical Review. *Biophys J* **1997**, *72*, 1047–1069.
- (26) Dill, K.; Bromberg, S. Molecular Driving Forces: Statistical Thermodynamics in Biology, Chemistry, Physics, and Nanoscience. **2010**.
- (27) Berendsen, H. J. C.; van der Spoel; van Drunen GROMACS: A Message-Passing Parallel Molecular Dynamics Implementation. *Computer Physics Communications* **1995**, *91*, 43–56.
- (28) Spoel, D.; Lindahl, E.; Hess, B.; Groenhof, G.; Mark, A.; Berendsen, H. GROMACS: Fast, Flexible, and Free. *J Comput Chem* **2005**, *26*, 1701–1718.

- (29) Wang, J.; Cieplak, P.; Kollman, P. How Well Does a Restrained Electrostatic Potential (RESP) Model Perform in Calculating Conformational Energies of Organic and Biological Molecules? *Journal of Computational Chemistry* **2000**, *21*, 1049–1074.
- (30) Hornak, V.; Abel, R.; Okur, A.; Strockbine, B.; Roitberg, A.; Simmerling, C. Comparison of Multiple Amber Force Fields and Development of Improved Protein Backbone Parameters.

 *Proteins: Structure, Function, and Bioinformatics 2006, 65, 712–725.
- (31) Schüttelkopf, A. W.; Aalten, D. M. F. van PRODRG: A Tool for High-Throughput Crystallography of Protein–ligand Complexes. *Acta Crystallographica Section D: Biological Crystallography* **2004**, *60*, 1355–1363.
- (32) Jorgensen, W.; Chandrasekhar, J.; Madura, J.; Impey, R.; Klein, M. Comparison of Simple Potential Functions for Simulating Liquid Water. *The Journal of Chemical Physics* **1983**, 79, 926–935.
- (33) Essmann, U.; Perera, L.; Berkowitz, M.; Darden, T.; Lee, H.; Pedersen, L. A Smooth Particle Mesh Ewald Method. *The Journal of Chemical Physics* **1995**, *103*, 8577–8593.
- (34) Hess, B.; Bekker, H.; Berendsen, H.; Fraaije, J. LINCS: A Linear Constraint Solver for Molecular Simulations. *Journal of Computational Chemistry* **1997**, *18*, 1463–1472.
- (35) Allen; Tildesley; Banavar, J. Computer Simulation of Liquids. *Physics Today* **1989**, *42*, 105–106.
- (36) Hockney, R. .; Goel, S. .; Eastwood, J. . Quiet High-Resolution Computer Models of a Plasma. *Journal of Computational Physics* **1974**, *14*, 148–158.
- (37) Bussi, G.; Donadio, D.; Parrinello, M. Canonical Sampling through Velocity Rescaling. *The Journal of Chemical Physics* **2007**, *126*, 014101.

- (38) Hoover, W. Canonical Dynamics: Equilibrium Phase-Space Distributions. *Physical Review A* **1985**, *31*, 1695–1697.
- (39) Nosé, S. A Molecular Dynamics Method for Simulations in the Canonical Ensemble. *Molecular Physics* **2006**, *52*, 255–268.
- (40) Still, C.; Tempczyk, A.; Hawley, R.; Hendrickson, T. Semianalytical Treatment of Solvation for Molecular Mechanics and Dynamics. *Journal of the American Chemical Society* **1990**, *112*, 6127–6129.
- (41) Schaefer, M.; Bartels, C.; Karplus, M. Solution Conformations and Thermodynamics of Structured Peptides: Molecular Dynamics Simulation with an Implicit Solvation Model. *Journal of Molecular Biology* **1998**, *284*, 835–848.
- (42) Spoel, D. van der; Lindahl, E.; Hess, B.; GROMACS development team *GROMACS User Manual Version 4.6.7*; 2014.
- (43) Onufriev, A.; Bashford, D.; Case, D. Exploring Protein Native States and Large-scale Conformational Changes with a Modified Generalized Born Model. *Proteins: Structure, Function, and Bioinformatics* **2004**, *55*, 383–394.
- (44) Torrie, G. M.; Valleau, J. P. Nonphysical Sampling Distributions in Monte Carlo Free-Energy Estimation: Umbrella Sampling. *Journal of Computational Physics* **1977**, *23*, 187–199.
- (45) Kumar, S.; Rosenberg, J.; Bouzida, D.; Swendsen, R.; Kollman, P. THE Weighted Histogram Analysis Method for Free-energy Calculations on Biomolecules. I. The Method. *Journal of Computational Chemistry* **1992**, *13*, 1011–1021.
- (46) Hub, J.; Groot, B.; Spoel, D. G_wham-A Free Weighted Histogram Analysis Implementation Including Robust Error and Autocorrelation Estimates. *Journal of Chemical Theory and Computation* **2010**, *6*, 3713–3720.

- (47) Neumann, R. Entropic Approach to Brownian Movement. *American Journal of Physics* **1980**, *48*, 354–357.
- (48) Yuan, C.; Li, S.; Zou, Q.; Ren, Y.; Yan, X. Multiscale Simulations for Understanding the Evolution and Mechanism of Hierarchical Peptide Self-Assembly. *Phys Chem Chem Phys* **2017**, *19*, 23614–23631.
- (49) Mason, T. O.; Michaels, T. C.; Levin, A.; Gazit, E.; Dobson, C. M.; Buell, A. K.; Knowles, T. P. Synthesis of Nonequilibrium Supramolecular Peptide Polymers on a Microfluidic Platform. *J. Am. Chem. Soc.* **2016**, *138*, 9589–96.
- (50) Wang, J.; Yuan, C.; Han, Y.; Wang, Y.; Liu, X.; Zhang, S.; Yan, X. Trace Water as Prominent Factor to Induce Peptide Self-Assembly: Dynamic Evolution and Governing Interactions in Ionic Liquids. *Small* **2017**, *13*, 1702175.
- (51) Zhang, B.; Liu, H.; Huang, X.; Dong, C.; Ren, J. Size Distribution of Nanoparticles in Solution Characterized by Combining Resonance Light Scattering Correlation Spectroscopy with Maximum Entropy Method (MEM-RLSCS). *Anal Chem* **2017**, *89*, 12609–12616.
- (52) Pal, N.; Verma, S.; Singh, M.; Sen, S. Fluorescence Correlation Spectroscopy: An Efficient Tool for Measuring Size, Size-Distribution and Polydispersity of Microemulsion Droplets in Solution. *Analytical Chemistry* **2011**, *83*, 7736–7744.
- (53) Sengupta, P.; Garai; Balaji; Periasamy; Maiti Measuring Size Distribution in Highly Heterogeneous Systems with Fluorescence Correlation Spectroscopy. *Biophysical Journal* **2003**, *84*, 1977–1984.
- (54) Mittag, J.; Milani, S.; Walsh, D.; Rädler, J.; McManus, J. Simultaneous Measurement of a Range of Particle Sizes during Aβ1–42 Fibrillogenesis Quantified Using Fluorescence Correlation Spectroscopy. *Biochemical and Biophysical Research Communications* **2014**.

- (55) Sahoo, B.; Balaji; Nag, S.; Kaushalya, S.; Maiti, S. Protein Aggregation Probed by Two-Photon Fluorescence Correlation Spectroscopy of Native Tryptophan. *The Journal of chemical physics* **2008**, *129*, 075103.
- (56) Garai, K.; Sureka, R.; Maiti Detecting Amyloid- Aggregation with Fiber-Based Fluorescence Correlation Spectroscopy. *Biophysical journal* **2007**, *92*, L55–L57.